



Metal-organic frameworks templated micropore-enriched defective MnCeO_x for low temperature chlorobenzene oxidation

Tong Chen^a, Rong Wang^a, Chen Sun^{a,*}, Debao Kong^a, Shengyong Lu^a, Xiaodong Li^a

^a State Key Laboratory of Clean Energy Utilization, Institute for Thermal Power Engineering, Zhejiang University, China

ARTICLE INFO

Keywords:

Metal-organic frameworks (MOFs)
Catalytic oxidation
Chlorobenzene
Micropore

ABSTRACT

In this study, a series of metal-organic frameworks (MOFs) derived binary porous MnCeO_x catalysts were synthesized via solvothermal method for chlorobenzene (CB) oxidation. Compared with the catalysts from coprecipitation and sol-gel method, Mn1Ce1-MOF catalyst presented the best performance with T_{90%} at 242 °C and highest CO_x yield of 94.6% at 400 °C, owing to its micropore-enriched structure, higher lattice oxygen ratio and better surface reducibility. The HCl selectivity of Mn1Ce1-MOF reached 91.3% at 400 °C. The gaseous byproducts over Mn1Ce1-MOF catalyst were identified and the degradation pathway of CB was proposed. The catalytic activity of Mn1Ce1-MOF catalyst at 300 °C could stabilize over 75% for 40 h. The oxidation of Mn³⁺ and chlorine species adsorption were considered to be the main reasons for the catalyst inactivation. This work provides a highly-efficient MOFs templated porous metal oxide for tail gas purification.

1. Introduction

Chlorinated volatile organic compounds (CVOCs) are extensively generated in various industrial processes such as petrochemical, paint and solvent manufacturing, which have aroused widespread concern about the environment and health because of their high toxicity, persistence and difficulty to biodegrade [1]. Hence, various methods to reduce CVOCs have been investigated. Low temperature (250~550 °C) catalytic oxidation is considered to be one of the most efficient and promising techniques [2]. Compared to direct thermal combustion, the catalytic oxidation of CVOCs to inorganic small molecules (such as HCl, CO₂ and H₂O) is an energy-efficient method for tail gas purification.

To date, zeolites [3,4], substrate supported noble metals [5,6] and transition metal oxides [7,8] were reported as the main catalytic materials in the CVOCs catalytic oxidation. For zeolites, their activities are related to their acid properties. However, the catalytic performances are easily affected by carbon deposition [9]. Supported noble metals can exhibit predominant activity towards CVOCs at micro dosage (0.1~0.5 wt%). However, the formation of toxic polychlorinated byproducts, rapid chlorine poisoning and high manufacturing cost restrict their massive real application [10]. Recently, more attention has been paid to transition metal oxides, owing to the low cost, good resistance to chlorine poisoning and excellent thermal stability [11]. The catalytic oxidation of CVOCs has been investigated over Fe₂O₃ [12], Co₃O₄ [13],

V₂O₅ [14], MnO_x [15] and CeO₂ [16] based catalysts.

Among them, manganese oxides show outstanding catalytic activity for CVOCs oxidation, because the redox cycle between Mn³⁺ and Mn⁴⁺ is conducive to active oxygen mobility and availability [17]. Nevertheless, the deactivation caused by chlorine poisoning can not be avoided [18]. The addition of other elements was reported to improve anti-poisoning ability of manganese oxides [19]. Cerium oxides have been extensively studied for the high oxygen storage capacity, good transfer ability and abundant oxygen vacancies [20]. It's reported that the adjunction of Mn could inhibit the Ce-Cl interaction via promoting Deacon reaction (4HCl + O₂ = 2H₂O + 2Cl₂) [21,22]. Du et al. [23] found that Ce and Mn had a significant effect in the adsorption and oxidation process of toluene respectively, the cooperation between the two elements improved the overall catalytic reaction. In the study of Wang et al. [24], MnO_x-CeO₂ catalyst exhibited 90% conversion of chlorobenzene at 236 °C, 170 °C lower than that of MnO_x. The excellent low-temperature activity of MnO_x-CeO₂ catalyst could be ascribed to sufficient active surface oxygen and better resistance to chlorine adsorption.

Recently, MOFs was reported to have remarkable potential application in heterogeneous catalysis, adsorption separation and sensing, due to their designable morphology and sizes, rich porous structure and polymetallic sites. MOFs derived mixed metal oxides could be promising catalysts for CVOCs oxidation, due to the advantages of controllable

* Corresponding author.

E-mail address: sunchen1@zju.edu.cn (C. Sun).

<https://doi.org/10.1016/j.apcata.2022.118845>

Received 12 June 2022; Received in revised form 13 August 2022; Accepted 23 August 2022

Available online 28 August 2022

0926-860X/© 2022 Elsevier B.V. All rights reserved.

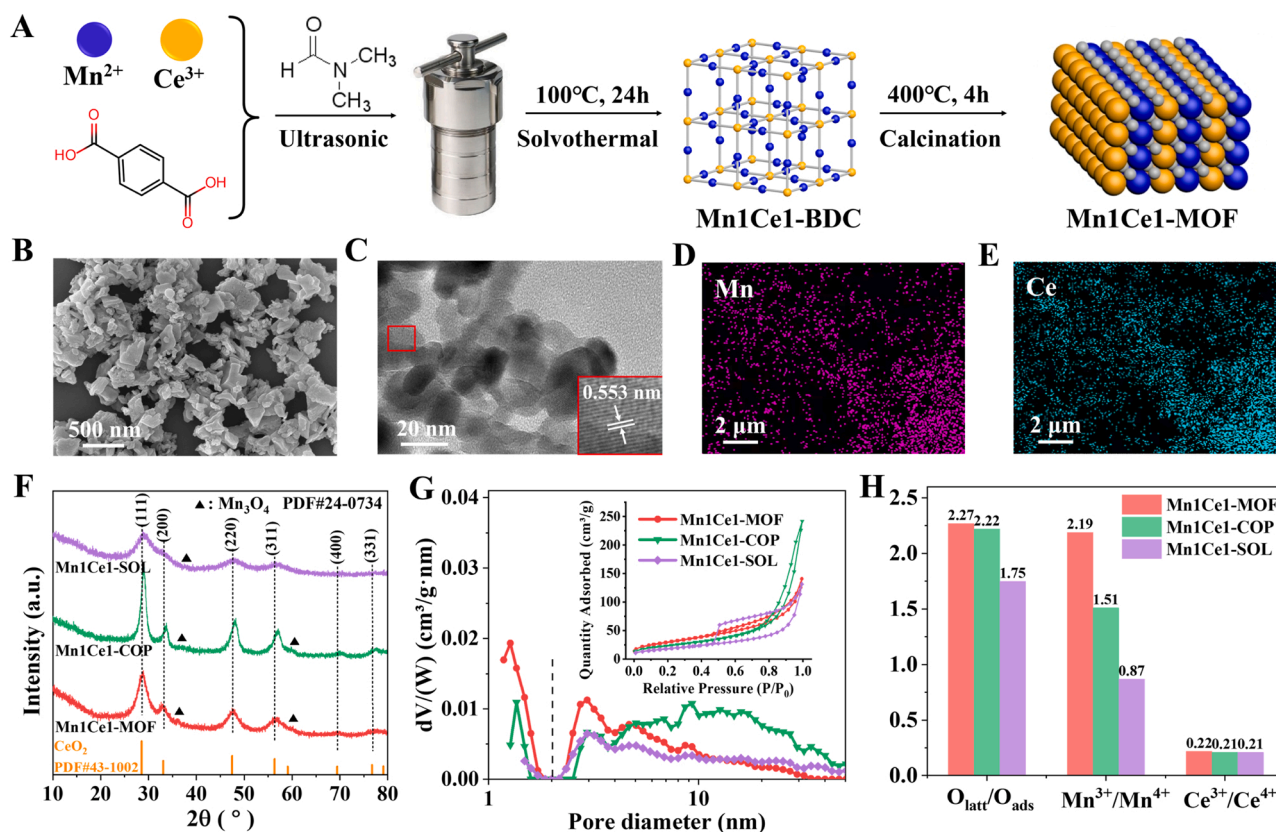


Fig. 1. Synthesis and characterization of MOFs derived catalysts. (A) synthesis route of Mn1Ce1-MOF, (B) SEM image, (C) TEM image and (D, E) element-mappings of Mn1Ce1-MOF catalyst, (F) XRD patterns, (G) pore diameter distributions (inlet: N_2 adsorption-desorption isotherms) and (H) elements valence calculation results derived from XPS spectra of MnCeO_x catalysts.

morphology, enhanced interaction between mixed metal oxides and rich porous structure. Li et al. [25] investigated the catalytic activity of CoCeO_x MOFs and Co₃O₄/CeO₂ nanocube for toluene oxidation. The CoCeO_x MOFs showed significantly better catalytic activity ($T_{50\%}$ and $T_{90\%}$ at 212 °C and 227 °C respectively) and complete oxidation ability at low temperature, profiting from more metal defects and oxygen vacancies. Zhang et al. [26] found that the MOFs templated rod-like MnCeO_x catalyst possessed better reducibility. In high humidity environment, adsorbed H₂O in the oxygen vacancies could facilitate the transformation from O_{ads} to O_{latt} and the mineralization of toluene. Hu et al. [27] reported that MOFs-templated MnO_x/Co₃O₄-4 h catalyst exhibited 90% CB conversion at 334 °C (1000 ppm, GHSV=60000 h⁻¹). The enhanced performance was mainly attributed to unique porous structure, rich defects and high lattice oxygen ratio.

In this study, we developed MOFs derived binary MnCeO_x catalysts by solvothermal method and explored their catalytic performance for CB oxidation compared with the catalysts from conventional co-precipitation and sol-gel method. The catalyst morphology, crystal structure, redox property, surface acidity and chemical composition of samples were characterized. The catalytic activity, selectivity, intermediate products distribution and long-time stability were comprehensively studied. Possible degradation pathway of CB over MOFs derived MnCeO_x catalyst was summarized. Finally, the used catalyst was characterized to find out the reasons for the decreased activity.

2. Materials and method

2.1. Catalysts preparation

Manganese (II) nitrate solution (Mn(NO₃)₂, 50 wt%), Manganese (II) acetate tetrahydrate ((CH₃COO)₂Mn·4H₂O, 99.0%), N,N-

dimethylformamide (DMF, 99.5%), absolute ethanol (C₂H₆O, 99.7%) and sodium hydroxide (NaOH, 96%) were purchased from Sinopharm Chemical Reagent Co., Ltd. Cerium (III) nitrate hexahydrate (Ce(NO₃)₃·6H₂O, 99.9%) were purchased from Aladdin. Terephthalic acid (H₂BDC, 98%) and citric acid (C₆H₈O₇, 99.5%) were purchased from Macklin.

As shown in Fig. 1A, MOFs derived catalysts were synthesized via the solvothermal method. Take Mn1Ce1-MOF as an example, 0.43 g Ce(NO₃)₃·6H₂O and 0.25 g (CH₃COO)₂Mn·4H₂O were dissolved in 30 mL DMF under magnetic stirring for 20 min. Similarly, 0.5 g H₂BDC was dissolved in 30 mL DMF. The above two solutions together with 10 mL deionized water were blended thoroughly under ultrasonication for 30 min. The resultant was transferred into a 100 mL stainless steel autoclave and reacted at 100 °C for 24 h in oven. After cooling to environmental temperature, the white precipitate was centrifuged and washed twice with DMF and ethanol. The MOFs template after drying at 100 °C for 12 h was named Mn1Ce1-BDC. Finally, Mn1Ce1-MOF was obtained by calcinating Mn1Ce1-BDC under air atmosphere at 400 °C for 4 h. Mn1Ce2-MOF and Mn2Ce1-MOF were synthesized in the same way with the molar ratio of Mn/Ce = 1:2 and 2:1 respectively.

For comparison, Mn1Ce1-COP and Mn1Ce1-SOL were synthesized by the traditional co-precipitation and sol-gel methods.

- (1) Mn1Ce1-COP: Same molar amount of Mn(NO₃)₂ and Ce(NO₃)₃·6H₂O were dissolved in deionized water. 2 M NaOH solution was dropwise added into the above solution at 50 °C until pH value reached 11, then the resultant was matured at 50 °C for 2 h. The sediments were centrifuged, washed with deionized water, and put into oven to dry at 100 °C for 12 h. Mn1Ce1-COP was obtained by calcinating the sediments in air atmosphere at 400 °C for 4 h.

(2) Mn1Ce1-SOL: Same molar amount of $\text{Mn}(\text{NO}_3)_2$ and $\text{Ce}(\text{NO}_3)_3 \cdot 6\text{H}_2\text{O}$ (both 0.4 mol L^{-1}) were dissolved in absolute ethanol. Same molar amount of citric acid was dissolved in absolute ethanol (1 mol L^{-1}). The above two solutions were mixed and sealed with plastic wrap. The mixture was put into the oven at $60 \text{ }^\circ\text{C}$ for 5 h to gelation. The gel was dried at $100 \text{ }^\circ\text{C}$ for 12 h followed by calcinating the gel in air atmosphere at $400 \text{ }^\circ\text{C}$ for 4 h.

2.2. Catalysts characterization

Scanning electron microscope (SEM) images were observed on a ZEISS GEMINI 300 scanning microscope operated at an accelerating voltage of 5 kV. Transmission Electron Microscope (TEM) images were obtained on a HT-7700 electron microscope operated at 100 kV. EDS elemental mapping were recorded on a Hitachi SU-8010 scanning electron microscope coupled with Oxford X-max 80 energy spectrometer. X-ray Powder diffraction (XRD) patterns were obtained on a Panalytical X'Pert'3 Powder with a $\text{CuK}\alpha$ radiation (40 kV , $\lambda = 1.5406 \text{ \AA}$, scanning step = 0.013°). Diffraction data were collected with the 2θ ranged from 10° to 80° with a scanning rate of 5° min^{-1} . Elemental composition analysis was measured by inductively coupled plasma optical emission spectroscopy (ICP-OES) technique on Agilent 720ES after digested in microwave digestion system. Nitrogen adsorption-desorption isotherms were obtained by Micromeritics ASAP 2460 at 77.3 K . 0.2 g of samples were outgassed at $200 \text{ }^\circ\text{C}$ for 8 h to eliminate water and other adsorbed impurities. The specific surface area was calculated using the Brunauer-Emmett-Teller (BET) approach, pore volume and pore size distribution was obtained via Discrete Fourier Transform (DFT) approach. X-ray photoelectron spectroscopy (XPS) spectra were recorded on a Thermo Scientific K-Alpha spectrometer using mono AlK α (1486.6 eV) radiation. The results were calibrated for charge effects by setting the binding energy of adventitious carbon (C1s) to 284.8 eV . The spectra were peak fitted using the Avantage 5.52 program. The background was subtracted with Smart-type pattern and the curve fitting was fixed in L/G mix of 30 %.

Hydrogen temperature-programmed reduction (H_2 -TPR) was performed on a BelCata II instrument equipped with a thermal conductivity detector (TCD). 50 mg of samples were pretreated in Ar flow at $150 \text{ }^\circ\text{C}$ for 1 h prior to run. After the samples were cooled down to $50 \text{ }^\circ\text{C}$, $10 \text{ } \%$ H_2/N_2 mixture flow (30 mL min^{-1}) was introduced and the reactor was heated at a rate of $10 \text{ }^\circ\text{C min}^{-1}$ from $50 \text{ }^\circ\text{C}$ to $800 \text{ }^\circ\text{C}$. Reduction of CuO to metal Cu was used to calibrate the H_2 consumption. NH_3 temperature-programmed desorption (NH_3 -TPD) was performed on a BelCata II instrument equipped with an online mass analyzer (Bel Mass). 100 mg of samples were pretreated in Helium flow (30 mL min^{-1}) at $300 \text{ }^\circ\text{C}$ for 1 h and then cooled down to $50 \text{ }^\circ\text{C}$. $10 \text{ } \%$ NH_3/He mixture gas was introduced for 1 h until saturation. Helium flow was introduced for 1 h to remove the weakly physically adsorbed NH_3 on the surface. Finally, the signal of desorbed gas (NH_3 , $m/z = 16$) was measured and recorded by MS in Helium atmosphere with a heating rate of $10 \text{ }^\circ\text{C min}^{-1}$ to $700 \text{ }^\circ\text{C}$. Temperature-programmed oxidation (TPO) was performed on a BelCata II instrument equipped with an online mass analyzer (Bel Mass). 50 mg of samples were placed in a reaction tube and pretreated from room temperature to $300 \text{ }^\circ\text{C}$ at $10 \text{ }^\circ\text{C min}^{-1}$. After being purged for 1 h with Helium gas flow (50 mL min^{-1}), samples were cooled to $50 \text{ }^\circ\text{C}$. $10 \text{ } \%$ O_2/He mixed gas (50 mL min^{-1}) was introduced for 1 h for saturated

adsorption, then the temperature was raised to $700 \text{ }^\circ\text{C}$ at $10 \text{ }^\circ\text{C min}^{-1}$, and the exhaust gas was detected by MS.

In situ DRIFTS were performed on a Nicolet 6700 FT-IR spectrometer equipped with an MCT detector. The sample was loaded into a stainless-steel reaction cell with a CaF_2 window and then preheated in a He atmosphere (30 mL min^{-1}) at $400 \text{ }^\circ\text{C}$ for 1 h. During the cooling process, the background infrared spectra were collected at $150 \text{ }^\circ\text{C}$, $250 \text{ }^\circ\text{C}$ and $350 \text{ }^\circ\text{C}$, respectively. Subsequently, the CB mixed gas (150 ppm , $11 \text{ } \%$ O_2 and He balance) was introduced and the real-time infrared spectrum of the reaction was recorded.

2.3. Catalytic activity test

Schematic diagram of CB catalytic oxidation experimental device was shown in Fig. S1. The catalytic activity, selectivity and stability test of MnCeO_x catalysts were performed in a fixed bed reactor at atmospheric pressure. Chlorobenzene solution (Sinopharm) was bubbled with a mixed air ($11 \text{ } \%$ $\text{O}_2/89 \text{ } \%$ N_2), which was fixed in 100 mL min^{-1} with digital mass flow controllers, controlling initial CB concentration at 150 ppm . Typically, 0.2 g of catalyst powder was diluted with quartz sand and filled into the quartz tube reactor (outer diameter 10 mm , inner diameter 8 mm). The reaction temperature was raised from $150 \text{ }^\circ\text{C}$ to $400 \text{ }^\circ\text{C}$, which was controlled with a temperature programmed system in vertical tubular furnace. The connecting pipes were wrapped by heating tape fixed in $150 \text{ }^\circ\text{C}$ to avoid condensation of CB. Outlet gases were monitored on-line using a gas chromatograph (Thermal Scientific TRACE 1300) equipped with a flame ionization detectors (FID) to detect the organic products. The concentration of CO, CO_2 and HCl in the exhaust air were detected with a Fourier Transform Infrared Spectrometer gas analyzer (FTIR, DX4000 Gasmet). The intermediate products at $T_{90\%}$ were first captured using an adsorption tube (Tenax TA) for 20 min and then released into a Gas Chromatograph-Mass Spectrometer analyzer (Agilent 7890 A GC and Agilent 5975 C MS) equipped with a thermal desorption instrument (PERSEE-TD7). The CB conversion, CO_x yield and HCl selectivity were calculated by Eqs. (1–3), respectively:

$$\text{CB conversion} = \frac{[\text{CB}]_{\text{in}} - [\text{CB}]_{\text{out}}}{[\text{CB}]_{\text{in}}} \times 100\% \quad (1)$$

$$\text{CO}_x \text{ yield} = \frac{[\text{CO}_2]_{\text{out}} + [\text{CO}]_{\text{out}}}{6[\text{CB}]_{\text{in}}} \times 100\% \quad (2)$$

$$\text{HCl selectivity} = \frac{[\text{HCl}]_{\text{out}}}{[\text{CB}]_{\text{in}}} \times 100\% \quad (3)$$

Where $[\text{CB}]_{\text{in}}$ and $[\text{CB}]_{\text{out}}$ are the stable concentrations of CB at the reactor inlet and outlet. $[\text{CO}_2]_{\text{out}}$, $[\text{CO}]_{\text{out}}$ and $[\text{HCl}]_{\text{out}}$ are the stable concentrations of CO_2 , CO and HCl at the reactor outlet.

3. Results and discussion

3.1. Catalysts characterization

3.1.1. Morphology analysis

SEM and TEM techniques were employed to observe the morphology feature of samples. As shown in Fig. 1B, Mn1Ce1-MOF presented uneven blocks. The TEM image of Mn1Ce1-MOF (Fig. 1C) displayed that the

Table 1
Structure parameter, elemental composition and activity of MnCeO_x catalysts.

Sample	Crystal size (nm)	S_{BET} (m^2/g)	Micropore area (m^2/g)	Pore volume (cm^3/g)	Average pore size (nm)	Mn/Ce molar ratio by ICP	Conversion ($^\circ\text{C}$)	
							$T_{50\%}$	$T_{90\%}$
Mn1Ce1-MOF	2.9	109.2	10.8	0.22	7.98	1.03	185	242
Mn1Ce1-COP	4.8	85.7	3.1	0.37	17.44	1.03	235	350
Mn1Ce1-SOL	2.1	67.6	0.7	0.20	12.03	1.06	217	294

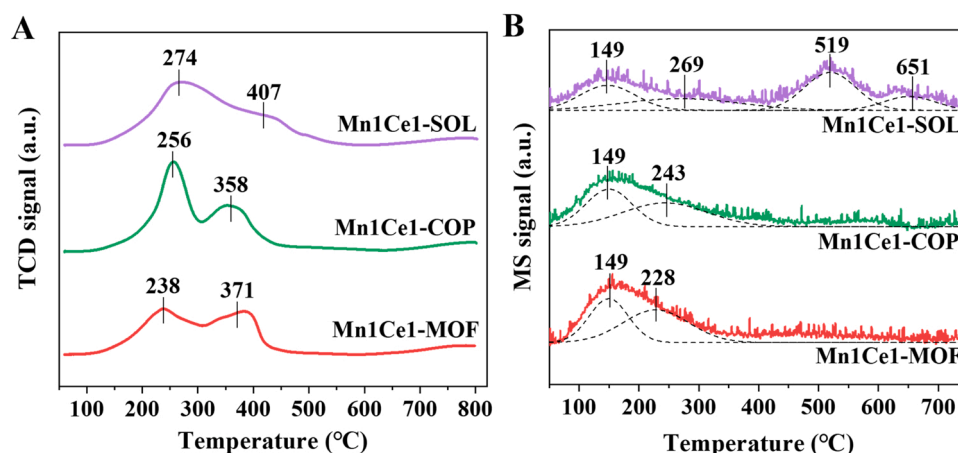


Fig. 2. (A) H₂-TPR profiles and (B) NH₃-TPD-MS profiles of MnCeO_x catalysts.

lattice spacing of the mainly exposed face was 0.553 nm, consistent with the result in Ref. [28]. It was speculated that the formation of solid solution interfered the original growth of the crystal, resulting in the lattice spacing to be larger than (111) lattice spacing of CeO₂ (0.312 nm, PDF# 43–1002). Mn1Ce1-COP (Fig. S2A) exhibited agglomerated spheres and Mn1Ce1-SOL (Fig. S2B) presented unique spatial coral structures. Fig. S2E and F showed that the morphology of MOFs derived MnCeO_x gradually transferred from irregular block to smaller spherical particle with increasing Mn content, and presented an agglomeration phenomenon. The element-mapping results shown in Fig. 1D and E revealed the homogeneous Mn and Ce distribution over the entire catalyst powder.

3.1.2. Physical properties

Fig. 1F displayed the XRD patterns of MnCeO_x catalysts, and the crystal sizes calculated by Scherrer formula were summarized in Table 1. Mn1Ce1-MOF, Mn1Ce1-COP and Mn1Ce1-SOL consisted of the same phase composition. It could be observed that peaks of all samples exhibited similar distribution and well coincided with the standard card. The peaks at 28.5°, 33.1°, 47.5°, 56.3°, 69.4°, 76.7° corresponded to (111), (200), (220), (311), (400) and (331) lattice planes of CeO₂ (PDF# 43–1002). The peaks at 36.1° and 59.8° corresponded to (211) and (224) lattice planes of Mn₃O₄ (PDF# 24–0734). Among them, the diffraction peaks of Mn1Ce1-SOL possessed weaker intensity and larger FWHM (full width at half maximum), indicating smaller crystal size (2.1 nm) and weaker crystallinity, which was confirmed by Scherrer formula calculation result and TEM image. For Mn1Ce2-MOF, Mn1Ce1-MOF and Mn2Ce1-MOF (Fig. S3A), the peaks belonged to Mn₃O₄ gradually strengthened and the average crystal size declined with increasing Mn content, which was consistent with TEM results. The shift and vanishment of some CeO₂ and Mn₃O₄ peaks may be ascribed to the existence of solid solution. As the ion radius of Mn³⁺ (0.066 nm) is slightly less than Ce⁴⁺ (0.094 nm), Mn is apt to join CeO₂ lattice to generate solid solution [29]. The Mn-Ce solid solution would disrupt the ordered growth of crystals, leading to the formation of defects (oxygen vacancies), which is conducive to CB catalytic oxidation [30,31].

ICP-OES was utilized to measure the elements contents of samples and the results were summarized in Table 1. The Mn/Ce molar ratio in all samples were equivalent to the design value, indicating that all samples were successfully synthesized by the adopted methods.

Fig. 1G displayed the pore diameter distributions and the N₂ adsorption-desorption isotherms of three MnCeO_x catalysts. It's proposed that micropores may be more crucial than mesopores during CB adsorption [32]. According to Fig. 1G, the pore diameter distribution of Mn1Ce1-MOF mainly concentrated at 1.27 nm, which is more approximate to the kinetic diameter of CB (0.78 nm), while Mn1Ce1-COP and Mn1Ce1-SOL possessed more mesopores above 3 nm. This character led

to larger adsorption potential between CB and catalysts by the overlapping van der Waals potential field, which is benefit for the catalytic oxidation process. Similar pore size distribution could be observed in three MOFs derived catalysts (Fig. S3B), mainly centered around 1.27 and 2.73 nm. All samples exhibited type IV isotherm with H4 hysteresis loop, confirming the co-existence of micropores and mesopores.

The BET specific surface area (S_{BET}), micropore area, total pore volume and average pore size of MnCeO_x catalysts were summarized in Table 1. Compared with Mn1Ce1-COP and Mn1Ce1-SOL, Mn1Ce1-MOF possessed largest S_{BET} (109.2 m²/g) and micropore area (10.8 m²/g), which could offer more active centers for catalytic reactions and improve the adsorption capacity [33,34]. For Mn1Ce2-MOF, Mn1Ce1-MOF and Mn2Ce1-MOF, in pace with increasing Mn content, S_{BET} declined and average pore size increased, but pore volume almost remained unchanged. The addition of Ce was reported to restrain the collapse and shrinkage of crystals structure during calcination [35]. Especially for MOFs derived catalysts, Ce was able to enter the pore access of MOFs and work as internal support to a certain degree.

3.1.3. Surface chemistry

The surface chemical compositions and states of all samples were examined by means of XPS characterization. Fig. S4 showed the profiles of O1s, Mn2p, Ce3d spectra and valence calculation results were displayed in Fig. 1H. The O1s spectra (Fig. S4A) was divided into two peaks at binding energy of 529.2 and 531.3 eV, which were attributed to the lattice oxygen (O_{latt}) and surface adsorbed oxygen (O_{ads}) [26]. It could be found from Fig. 1H that the O_{latt}/O_{ads} values of Mn1Ce1-MOF (2.27) was higher than that of Mn1Ce1-COP (2.22) and Mn1Ce1-SOL (1.75), indicating that lattice oxygen were the major species in Mn1Ce1-MOF and Mn1Ce1-COP. The catalytic oxidation process of CVOs over transition metal oxides generally obeyed the Mars-Van-Krevelen mechanism. The oxygen species follow the transformation route: O₂(ads)→O²⁻(ads)→O⁻(ads)→O²⁻(latt), and more lattice oxygen species in MOFs derived catalysts was conducive to the break of C-H bonds [36].

The Mn2p spectra (Fig. S4B) exhibited two compositions of Mn2p 3/2 and Mn2p 1/2 at binding energy of 641.3 and 653 eV. The peak of Mn2p 3/2 could be further fitted into three peaks of Mn³⁺, Mn⁴⁺ and satellite at binding energy of 640.9, 642.4 and 645.1 eV, respectively [37]. The satellite peaks were generally created by the collision of excited electrons and valence electrons in transition metal oxides. The coexistence of Mn³⁺ and Mn⁴⁺ suggested that the Mn consisted of mixed valence states in all samples, among them Mn³⁺ may originate from the oxygen vacancies generated by crystal defects. The presence of Mn³⁺ could facilitate electron transfer and promote the catalytic reaction cycle due to better reducibility [38]. As shown in Fig. 1H, the Mn³⁺/Mn⁴⁺ values of Mn1Ce1-MOF, Mn1Ce1-COP and Mn1Ce1-SOL were 2.19, 1.51 and 0.87, respectively. Hence the highest Mn³⁺/Mn⁴⁺ value of

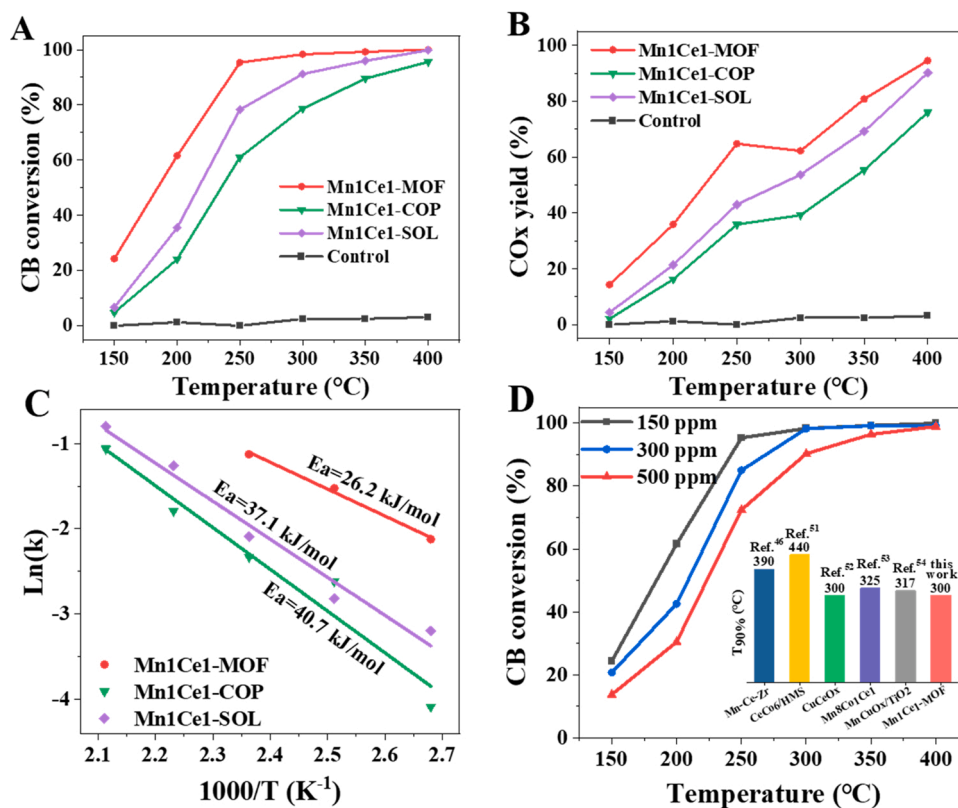


Fig. 3. (A) catalytic activities, (B) CO_x yields, (C) Arrhenius plots of MnCeO_x catalysts (150 ppm CB, WHSV = 30,000 mL g⁻¹ h⁻¹), (D) catalytic activities for Mn1Ce1-MOF at different CB concentrations (inlet: T_{90%} of CB oxidation at 1000/500 ppm over Mn-based or Ce-based published catalysts).

Mn1Ce1-MOF indicated the best reducibility among the catalysts.

The Ce3d spectra (Fig. S4C) could be deconvoluted into eight peaks. The peaks at binding energy of 882, 888.7, 897.9, 900.5, 907.3 and 916.2 eV matched up with Ce⁴⁺, and the peaks at binding energy of 885 and 902.8 eV matched up with Ce³⁺. It could be found from Fig. 1H that the Ce³⁺/Ce⁴⁺ values of all samples were all around 0.21, which showed that synthesis method had little impact on Ce³⁺/Ce⁴⁺ value in this study.

3.1.4. Reducibility properties

H₂-TPR was tested to determine the reducibility properties of MnCeO_x catalysts and the profiles were displayed in Fig. 2A. The first peak at 230~270 °C originated from the reduction of MnO₂/Mn₂O₃ to Mn₃O₄, and the second peak at 330~400 °C originated from the reduction of Mn₃O₄ to MnO and the surface oxygen from CeO₂ [27,39]. Low temperature reducibility reflected the mobility of oxygen species actually participating in the catalytic reaction, which is essential for the catalytic oxidation [40,41]. As shown in Fig. 2A, the first peak temperature (238 °C) of Mn1Ce1-MOF was lower than that of Mn1Ce1-COP (256 °C) and Mn1Ce1-SOL (270 °C), which revealed the intensified mobility of oxygen species in MOFs derived metal oxide [42,43]. The strong interaction between Ce and Mn has been reported to reduce the binding energy of cations and oxygen, resulting in higher oxygen mobility [44]. The H₂ consumption followed the sequence: Mn1Ce1-SOL (2.39 mmol/g) > Mn1Ce1-COP (2.17 mmol/g) > Mn1Ce1-MOF (1.71 mmol/g), which was consistent with XPS results. As for three MOFs derived catalysts, the initial temperature and intensity of the two reduction peaks increased significantly with the increase of Mn content, which suggested that Mn species might be more responsible for the catalyst reducibility (Fig. S5A).

3.1.5. Acidity properties

Acidity properties of the catalysts are crucial for chlorinated organic pollutant oxidation process. The breaking of C-Cl bond in CB usually

occurred at acidic sites, and enhanced acidity could accelerate the removal of reactive chlorine. Acidity properties of samples were measured by NH₃-TPD-MS. The acidic sites were generally classified into weak acidity (< 200 °C), moderate acidity (200~400 °C) and strong acidity (> 400 °C) [45]. As shown in Fig. 2B, all samples exhibited NH₃ desorption peaks at 149 °C and 228~269 °C. Moderate acidity played a more important role than weak acidity, among them Mn1Ce1-MOF possessed the most moderate acidities, which was conducive to CB catalytic oxidation.

3.2. Catalytic activity and selectivity

Fig. 3A showed the catalytic activities of MnCeO_x catalysts for CB oxidation over 150~400 °C range. In order to find out whether CB would be removed without catalyst, pure quartz was tested as control. As a result, almost no CB was removed even at temperature up to 400 °C. It was indicated that CB cannot be effectively oxidized without catalyst under the selected conditions. All samples exhibited a conspicuous upward trend in the range of 150~250 °C. According to Fig. 3A, the T_{90%} of samples followed the order: Mn1Ce1-MOF (242 °C) < Mn1Ce1-SOL (294 °C) < Mn1Ce1-COP (350 °C). Mn1Ce1-MOF catalyst had the best performance, when the temperature reached 185 °C and 242 °C, 50% and 90% CB removal were achieved respectively. According to above characterization analysis, the best catalytic performance of Mn1Ce1-MOF may be ascribed to the micropore-enriched structure, higher lattice oxygen ratio and better surface reducibility. The suitable pore structure of MOFs derived catalyst enhanced the CB adsorption, while the enhanced interaction between Ce and Mn was responsible for the surface reducibility. Mn/Ce ratio was reported to dramatically influence the catalytic performance [46]. Therefore, we prepared three MOFs derived catalysts with various Mn/Ce ratio, and the results in Fig. S6A showed that the appropriate ratio of Mn/Ce is 1:1.

As shown in Fig. 3B and Fig. S6B, CO_x yield curves of all catalysts

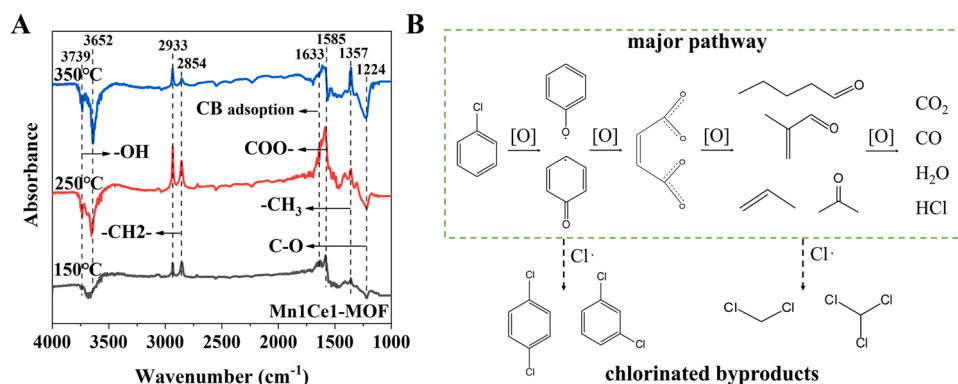


Fig. 4. (A) In situ DRIFTS spectra and (B) possible degradation pathway of CB oxidation over Mn1Ce1-MOF catalyst.

were lagging to the conversion efficiency, indicating the incomplete combustion of CB at low temperature. In the temperature range studied, the CO_x yield of Mn1Ce1-MOF consistently far exceeds Mn1Ce1-COP and Mn1Ce1-SOL. The Mn1Ce1-MOF catalyst presented the highest CO_x yield of 94.6% at 400 °C, which was much higher than that of Mn1Ce1-COP (76%). It was reported that reactive chlorine species are prone to be adsorbed on the catalyst surface, leading to a decrease in oxygen mobility so that the intermediates cannot be completely mineralized to CO₂ [47]. With the temperature increasing, part of the adsorbed chlorine species could be removed through Deacon reaction or the intermediates chlorination [48]. Therefore, the deposition of chlorine species resulted in a transient decrease at about 300 °C on the CO_x yield curves of Mn1Ce1-MOF. A similar phenomenon could also be found in the reported study [18].

Apparent activation energy reflects the difficulty of catalytic reaction at low temperature. It was assumed that the oxidation of CB followed a first-order kinetic mechanism, and the Arrhenius function was used to calculate the apparent activation energy for conversion (E_a). As shown in Fig. 3C, the E_a values of MnCeO_x catalysts followed the order: Mn1Ce1-MOF (26.2 kJ/mol) < Mn1Ce1-SOL (37.10 kJ/mol) < Mn1Ce1-COP (40.73 kJ/mol). The E_a values of MOFs derived catalysts (Fig. S6C) were generally lower than Mn1Ce1-SOL and Mn1Ce1-COP, indicating the better catalytic activity. Fig. S6D showed the HCl selectivities of Mn1Ce1-MOF, Mn1Ce1-COP and Mn1Ce1-SOL. The HCl selectivities of all samples were lower than conversion ratios, demonstrating that part of the chlorine may exist in chlorinated by-products or on the catalyst surface. Mn1Ce1-SOL presented the highest HCl selectivity at all temperatures from 150° to 400 °C, which could be ascribed to the strong acidic sites [49,50]. The HCl selectivities of Mn1Ce1-SOL and Mn1Ce1-MOF reached 94 % and 91.3 % at 400 °C, respectively, which was higher than that of Mn1Ce1-COP (77.3 %). These results demonstrated that Mn1Ce1-MOF exhibited excellent dichlorination capacity for CB.

The CB catalytic performances of Mn1Ce1-MOF at different CB concentrations were shown in Fig. 3D, 90 % conversion was achieved at 270 °C for 300 ppm and 300 °C for 500 ppm respectively. Fig. 3D inlet and Table S3 summarized some published work for CB catalytic oxidation over Mn-based or Ce-based catalysts [46,51–54]. It could be found that Mn1Ce1-MOF catalyst is effective for CB oxidation compared with other catalysts.

3.3. Oxidation intermediate and proposed degradation pathway

The gaseous intermediate products at T_{90%} over Mn1Ce1-MOF were analyzed by GC-MS. As shown in Fig. S7 and Table S4, thirteen organic compounds were distinguished and ranked by retention time. The major intermediate products approximately include nonchlorinated hydrocarbons (propene), aromatic hydrocarbon (benzene), ketone (acetone, methacrolein and pentanal). In addition, five chlorinated hydrocarbons

(dichloromethane, trichloromethane, tetrachloromethane, trichloroethylene and perchloroethylene) and three chlorinated aromatic hydrocarbons (chlorobenzene, 1,4-dichlorobenzene and 1,3-dichlorobenzene) were also found in the outlet gas. The presence of chlorination compounds might originate from the electrophilic chlorination reaction of adsorbed Cl⁻ species with intermediates. Such phenomenon were also observed in catalytic process of chlorinated hydrocarbons over molecular sieve [49], supported noble metals [6] and other transition metal oxides [33,46].

In situ DRIFTS measurements were conducted to probe the CB degradation pathway at different temperatures. Fig. 4A presented the infrared spectra over Mn1Ce1-MOF catalyst at 150 °C, 250 °C and 350 °C. Obvious vibration bands were observed at 1224, 1357, 1585, 1633, 2854, 2933, 3652 and 3739 cm⁻¹. The peak at 1633 cm⁻¹ was corresponded to the CB adsorption on acidic sites [55], the intensity increased at first and decreased due to the enhanced oxidative capacity with increasing temperature. The negative peak at 1224 cm⁻¹ was attributed to C-O stretching vibrations of phenolic species [56]. The band at 1585 cm⁻¹ was commonly assigned to COO- stretching vibrations of maleate and acetate [57]. The peak at 1357 cm⁻¹ was associated with -CH₃ stretching vibration of acetate [58]. The peaks at 2854 and 2933 cm⁻¹ was attributed to -CH₂- stretching vibration band of aromatic ring [59]. It was observed that the bands of 1585, 2854 and 2933 cm⁻¹ decreased when the temperature was increased to 350 °C, which indicated that the aromatic ring, maleate and acetate were further oxidized to low-carbon species. The negative peaks at 3652 and 3739 cm⁻¹ were due to the consumption of hydroxyl [55], and more and more hydroxyl groups participated in the oxidation reaction with increasing temperature. Similar infrared spectra were observed over Mn1Ce1-COP and Mn1Ce1-SOL catalysts (Fig. S8), indicating the similar degradation pathway. Furthermore, the intensities of intermediates and the consumption of hydroxyl groups over Mn1Ce1-MOF were much higher than that of Mn1Ce1-COP and Mn1Ce1-SOL at the same temperature, which may explain the best catalytic activity of Mn1Ce1-MOF among three MnCeO_x catalysts.

Based on the GC-MS byproducts and in situ DRIFTS analysis above, possible degradation pathway of CB over Mn1Ce1-MOF catalyst was displayed in Fig. 4B. Firstly, CB molecules were adsorbed on the surface acid sites. The C-Cl bonds were preferentially broken over C-H bonds due to the lower binding energy, and phenolic compounds were formed through nucleophilic substitution. Under the attack of nucleophilic oxygen, the benzene ring was cleaved and the phenols were further oxidized into other intermediates, such as pentanal and methacrolein. At the same time, CH₂Cl₂, CHCl₃ and other chlorinated products were generated by electrophilic substitution if the Cl⁻ species reacted with the acetic anhydride [60]. Finally, the intermediates were decomposed into small inorganic molecules, including CO₂, CO, H₂O and HCl.

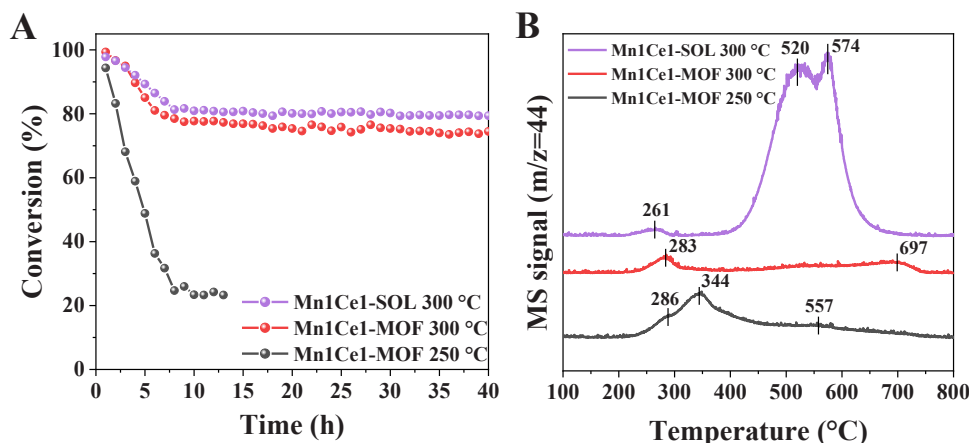


Fig. 5. (A) CB conversion versus reaction time, (B) MS signal of CO₂ in TPO test over used catalysts after stability test.

Table 2

Deposited coke and elements distribution derived from XPS spectra of used catalysts after stability test.

	deposited coke (mmol/gcat)	Mn ³⁺ /Mn ⁴⁺	
		fresh	used
Mn1Ce1-MOF 250 °C	0.15	2.19	0.87
Mn1Ce1-MOF 300 °C	0.07	2.19	1.37
Mn1Ce1-SOL 300 °C	0.5	0.87	0.93

3.4. Catalyst stability and deactivation mechanism

To explore the catalytic stability, Fig. 5A presented the CB conversion of Mn1Ce1-MOF at 250 °C and 300 °C and Mn1Ce1-SOL at 300 °C, respectively. For Mn1Ce1-MOF, the CB conversion at 250 °C rapidly dropped from 95.3 % to 20 % within 8 h. Conversely, the reaction efficiency at 300 °C slowly dropped within the first 7 h, from 98.4 % to 80 %, and then maintained at about 75 % in the following 40 h. The reaction efficiency of Mn1Ce1-SOL decreased at a slower rate than Mn1Ce1-MOF and eventually stabilized at about 80 %. To explore the reasons for decreased activity, the XPS and TPO characterization on the used catalysts were performed. According to the Mn2p fitting results in Fig. S9A and Table 2, the Mn³⁺/Mn⁴⁺ value of Mn1Ce1-MOF dropped from 2.19 to 1.37 and 0.87 at 300 °C and 250 °C respectively, indicating the oxidation of Mn³⁺, which resulted in decline of surface reducibility. It's reported that Deacon reaction and oxychlorination reaction might occur on transition metal oxides (especially Mn oxides), resulting in the formation of chlorinated hydrocarbons and toxic dichlorobenzene [47]. The Cl2p spectra showed that the catalyst after stability test contained chlorine species at binding energy of 198.4 and 200 eV attributed to Cl2p 3/2 and Cl2p 1/2 (Fig. S9B). The surface accumulating chlorine species competed with CB and oxygen molecules, which may lead to the decrease of catalyst activity [7]. The active sites were blocked and occupied by new substances, possibly MnCl_x or MnO_yCl_z [61].

Fig. 5B showed the MS signal of CO₂ in TPO test of three catalyst and the amount of deposited coke were summarized in Table 2. After 40 h operation at 300 °C, the TPO curve of used Mn1Ce1-SOL possessed the most intense peak of CO₂ signal at 520 and 574 °C, which could be ascribed to the deposited coke [62]. After integration, we calculated that 0.5 mmol/gcat deposited coke were detected. Excessive acidity was reported to cause coke deposition on the catalyst [63]. It could be inferred that the declined activity of Mn1Ce1-SOL at 300 °C could be ascribed to the coke deposition. As for the Mn1Ce1-MOF working at 250 °C, CO₂ signal reached a maximum at 344 °C, and the amount of deposited coke (0.15 mmol/gcat) was much higher than that of Mn1Ce1-MOF at 300 °C (0.07 mmol/gcat). The dual effects of coke deposition and reactive

chlorine adsorption resulted in the rapid deactivation of Mn1Ce1-MOF at 250 °C.

4. Conclusion

In this work, a series of MOFs derived binary porous MnCeO_x catalysts were prepared via solvothermal method for CB oxidation. Compared with the catalysts from traditional co-precipitation and sol-gel method, the Mn1Ce1-MOF catalyst presented the best performance with T_{90%} at 242 °C and the highest CO_x yield of 94.6% at 400 °C. The HCl selectivity of Mn1Ce1-MOF reached 91.3% at 400 °C. The remarkable activities could be ascribed to the micropore-enriched structure (micropore area 10.8 m²/g), higher lattice oxygen ratio and better surface reducibility. These characteristics enhanced the accumulation of pollutants and oxygen mobility, which finally increased the CB oxidation rate over Mn1Ce1-MOF at low temperature. Possible degradation pathway of CB over Mn1Ce1-MOF catalyst was proposed. The C-Cl bond of CB molecules adsorbed on surface acid sites were preferentially broken and phenolic compounds were attacked by nucleophilic oxygen to break the benzene ring and further oxidized into other intermediates, such as pentanal and methacrolein. Stability test displayed that the catalytic activity of Mn1Ce1-MOF catalyst at 300 °C could maintain above 75% in the following 40 h. The oxidation of Mn³⁺ and adsorbed surface chlorine species were responsible for the decrease of catalytic activity.

CRedit authorship contribution statement

Tong Chen: Methodology, Supervision, Writing – review & editing. **Rong Wang:** Methodology, Data curation, Writing – original draft. **Chen Sun:** Conceptualization, Reviewing, Supervision. **Debao Kong:** Methodology, Data curation. **Shengyong Lu:** Reviewing, Supervision. **Xiaodong Li:** Reviewing, Supervision.

Declaration of Competing Interest

The authors declare that they have no known competing financial interests or personal relationships that could have appeared to influence the work reported in this paper.

Data Availability

The authors do not have permission to share data.

Acknowledgments

This study is supported by the National Key Research and

Development Program of China (2018YFC1802103).

Appendix A. Supporting information

Supplementary data associated with this article can be found in the online version at doi:10.1016/j.apcata.2022.118845.

References

- [1] C. He, J. Cheng, X. Zhang, M. Douthwaite, S. Pattison, Z. Hao, *Chem. Rev.* 119 (2019) 4471–4568.
- [2] C. Zhang, Y. Wang, G. Li, L. Chen, Q. Zhang, D. Wang, X. Li, Z. Wang, *Appl. Surf. Sci.* 532 (2020), 147320.
- [3] L. Li, J. Shi, M. Tian, C. Chen, B. Wang, M. Ma, C. He, *Appl. Catal. B-Environ.* 282 (2021), 119565.
- [4] S. Scirè, S. Minicò, C. Crisafulli, *Appl. Catal. B-Environ.* 45 (2003) 117–125.
- [5] P. Topka, R. Delaigle, L. Kaluža, E.M. Gaigneaux, *Catal. Today* 253 (2015) 172–177.
- [6] Q. Dai, S. Bai, X. Wang, G. Lu, *Appl. Catal. B-Environ.* 129 (2013) 580–588.
- [7] D. Yu, W. Xingyi, L. Dao, D. Qiguang, *J. Hazard. Mater.* 188 (2011) 132–139.
- [8] T. Cai, H. Huang, W. Deng, Q. Dai, W. Liu, X. Wang, *Appl. Catal. B-Environ.* 166–167 (2015) 393–405.
- [9] X. Weng, P. Sun, Y. Long, Q. Meng, Z. Wu, *Environ. Sci. Technol.* 51 (2017) 8057–8066.
- [10] J.M. Giraudon, A. Elhachimi, G. Leclercq, *Appl. Catal. B-Environ.* 84 (2008) 251–261.
- [11] M.S. Kamal, S.A. Razzak, M.M. Hossain, *Atmos. Environ.* 140 (2016) 117–134.
- [12] Y. Wang, G. Wang, W. Deng, J. Han, L. Qin, B. Zhao, L. Guo, F. Xing, *Chem. Eng. J.* 395 (2020) 125–172.
- [13] Y. Lao, N. Zhu, X. Jiang, J. Zhao, Q. Dai, X. Wang, *Catal. Sci. Technol.* 8 (2018) 4797–4811.
- [14] C. Gannoun, A. Turki, H. Kochkar, R. Delaigle, P. Eloy, A. Ghorbel, E. M. Gaigneaux, *Appl. Catal. B-Environ.* 147 (2014) 58–64.
- [15] G. Chen, Z. Wang, F. Lin, Z. Zhang, H. Yu, B. Yan, Z. Wang, *J. Hazard. Mater.* 391 (2020), 122218.
- [16] Q. Dai, J. Wu, W. Deng, J. Hu, Q. Wu, L. Guo, W. Sun, W. Zhan, X. Wang, *Appl. Catal. B-Environ.* 249 (2019) 9–18.
- [17] Y. Dai, X. Wang, Q. Dai, D. Li, *Appl. Catal. B-Environ.* 111–112 (2012) 141–149.
- [18] X. Wang, L. Ran, Y. Dai, Y. Lu, Q. Dai, *J. Colloid Interf. Sci.* 426 (2014) 324–332.
- [19] A. Tang, L. Hu, X. Yang, Y. Jia, Y. Zhang, *Catal. Commun.* 82 (2016) 41–45.
- [20] Q. Wang, K.L. Yeung, M.A. Banares, *Catal. Today* 356 (2020) 141–154.
- [21] Q. Dai, S. Bai, Z. Wang, X. Wang, G. Lu, *Appl. Catal. B-Environ.* 126 (2012) 64–75.
- [22] P. Yang, Z. Shi, S. Yang, R. Zhou, *Chem. Eng. Sci.* 126 (2015) 361–369.
- [23] J. Du, Z. Qu, C. Dong, L. Song, Y. Qin, N. Huang, *Appl. Surf. Sci.* 433 (2018) 1025–1035.
- [24] X. Wang, Q. Kang, D. Li, *Catal. Commun.* 9 (2008) 2158–2162.
- [25] Y. Li, W. Han, R. Wang, L. Weng, A. Serrano-Lotina, M.A. Banares, Q. Wang, K. L. Yeung, *Appl. Catal. B-Environ.* 275 (2020), 119121.
- [26] X. Zhang, F. Bi, Z. Zhu, Y. Yang, S. Zhao, J. Chen, X. Lv, Y. Wang, J. Xu, N. Liu, *Appl. Catal. B-Environ.* (2021), 120393.
- [27] Z. Hu, J. Chen, D. Yan, Y. Li, H. Jia, C. Lu, *Appl. Surf. Sci.* 551 (2021), 149453.
- [28] Q. Wang, Y. Li, A. Serrano-Lotina, W. Han, R. Portela, R. Wang, M.A. Banares, K. L. Yeung, *J. Am. Chem. Soc.* 143 (2020) 196–205.
- [29] Z. Sibaib, F. Puleo, J.M. Garcia-Vargas, L. Retailleau, C. Descorme, L.F. Liotta, J. L. Valverde, S. Gil, A. Giroir-Fendler, *Appl. Catal. B-Environ.* 209 (2017) 689–700.
- [30] L. Niu, G. Xian, Z. Long, G. Zhang, N. Zhou, *J. Environ. Sci.* 89 (2020) 206–217.
- [31] L. Deng, Y. Ding, B. Duan, Y. Chen, P. Li, S. Zhu, S. Shen, *Mol. Catal.* 446 (2018) 72–80.
- [32] D.D. Do, H.D. Do, *AIChE J.* 48 (2002) 2213–2229.
- [33] W. Deng, Q. Tang, S. Huang, L. Zhang, Z. Jia, L. Guo, *Appl. Catal. B-Environ.* 278 (2020), 119336.
- [34] Z. Hu, Y. Zhu, Z. Gao, G. Wang, Y. Liu, X. Liu, Z. Yuan, *Chem. Eng. J.* 302 (2016) 23–32.
- [35] X. Chen, X. Chen, S. Cai, E. Yu, J. Chen, H. Jia, *Appl. Surf. Sci.* 475 (2019) 312–324.
- [36] Y. Zhang, Z. Tan, X. Wang, Y. Zhan, Y. Xiao, C. Au, L. Jiang, *Nanoscale* 11 (2019) 4794–4802.
- [37] Y. Ruan, H. Guo, J. Li, Z. Liu, N. Jiang, Y. Wu, *Chemosphere* 258 (2020), 127334.
- [38] F.N. Aguero, A. Scian, B.P. Barbero, L.E. Cadús, *Catal. Today* 133–135 (2008) 493–501.
- [39] H. Sun, X. Yu, X. Ma, X. Yang, M. Lin, M. Ge, *Catal. Today* 355 (2020) 580–586.
- [40] C.A. Chagas, E.F. de Souza, R.L. Manfro, S.M. Landi, M.M.V.M. Souza, M. Schmal, *Appl. Catal. B-Environ.* 182 (2016) 257–265.
- [41] J. Chen, X. Chen, X. Chen, W. Xu, Z. Xu, H. Jia, J. Chen, *Appl. Catal. B-Environ.* 224 (2018) 825–835.
- [42] J. Quiroz, J. Giraudon, A. Gervasini, C. Dujardin, C. Lancelot, M. Trentesaux, J. Lamonier, *ACS Catal.* 5 (2015) 2260–2269.
- [43] F.N. Aguero, A. Scian, B.P. Barbero, R. Brahmí, J. Giraudon, J. Lamonier, *J. Hazard. Mater.* 188 (2011) 422–427.
- [44] P. Venkataswamy, K.N. Rao, D. Jampaiah, B.M. Reddy, *Appl. Catal. B-Environ.* 162 (2015) 122–132.
- [45] Q. Dai, W. Wang, X. Wang, G. Lu, *Appl. Catal. B-Environ.* 203 (2017) 31–42.
- [46] G. Long, M. Chen, Y. Li, J. Ding, R. Sun, Y. Zhou, X. Huang, G. Han, W. Zhao, *Chem. Eng. J.* 360 (2019) 964–973.
- [47] Q. Dai, X. Wang, G. Lu, *Appl. Catal. B-Environ.* 81 (2008) 192–202.
- [48] S. Zweidinger, J.P. Hofmann, O. Balmes, E. Lundgren, H. Over, *J. Catal.* 272 (2010) 169–175.
- [49] P. Sun, S. Zhai, J. Chen, J. Yuan, Z. Wu, X. Weng, *Appl. Catal. B-Environ.* 272 (2020), 119015.
- [50] S. Cao, M. Shi, H. Wang, F. Yu, X. Weng, Y. Liu, Z. Wu, *Chem. Eng. J.* 290 (2016) 147–153.
- [51] W. Zhao, J. Cheng, L. Wang, J. Chu, J. Qu, Y. Liu, S. Li, H. Zhang, J. Wang, Z. Hao, T. Qi, *Appl. Catal. B-Environ.* 127 (2012) 246–254.
- [52] C. He, B. Xu, J. Shi, N. Qiao, Z. Hao, J. Zhao, *Fuel Process. Technol.* 130 (2015) 179–187.
- [53] J. Kan, L. Deng, B. Li, Q. Huang, S. Zhu, S. Shen, Y. Chen, *Appl. Catal.*, A. 530 (2017) 21–29.
- [54] V.H. Vu, J. Belkouch, A. Ould-Dris, B. Taouk, *J. Hazard. Mater.* 169 (2009) 758–765.
- [55] A.B. Ene, T. Archipov, E. Roduner, *J. Phys. Chem. C.* 115 (2011) 3688–3694.
- [56] S.L. Alderman, G.R. Farquar, E.D. Poliakov, B. Dellinger, *Environ. Sci. Technol.* 39 (2005) 7396–7401.
- [57] J. Lichtenberger, M.D. Amiridis, *J. Catal.* 223 (2004) 296–308.
- [58] X. Liu, L. Chen, T. Zhu, R. Ning, *J. Hazard. Mater.* 363 (2019) 90–98.
- [59] X. Weng, P. Sun, Y. Long, Q. Meng, Z. Wu, *Environ. Sci. Technol.* 51 (2017) 8057–8066.
- [60] P. Sun, W. Wang, X. Weng, X. Dai, Z. Wu, *Environ. Sci. Technol.* 52 (2018) 6438–6447.
- [61] C. Du, S. Lu, Q. Wang, A.G. Buekens, M. Ni, D.P. Debecker, *Chem. Eng. J.* 334 (2018) 519–544.
- [62] B. Sánchez, M.S. Gross, B.D. Costa, C.A. Querini, *Appl. Catal. A: Gen.* 364 (2009) 35–41.
- [63] Y. Su, K. Fu, C. Pang, Y. Zheng, C. Song, N. Ji, D. Ma, X. Lu, C. Liu, R. Han, Q. Liu, *Environ. Sci. Technol.* 14 (2022) 9854–9871.